

V. Lyakhovsky · S. Hurwitz · O. Navon

Bubble growth in rhyolitic melts: experimental and numerical investigation

Received: 19 June 1995 / Accepted: 27 December 1995

Abstract Bubble growth controlled by mass transfer of water from hydrated rhyolitic melts at high pressures and temperatures was studied experimentally and simulated numerically. Rhyolitic melts were hydrated at 150 MPa, 780–850 °C to uniform water content of 5.5–5.3 wt%. The pressure was then dropped and held constant at 15–145 MPa. Upon the drop bubbles nucleated and were allowed to grow for various periods of time before final, rapid quenching of the samples. The size and number density of bubbles in the quenched glasses were recorded. Where number densities were low and run duration short, bubble sizes were in accord with the growth model of Scriven (1959) for solitary bubbles. However, most results did not fit this simple model because of interaction between neighboring bubbles. Hence, the growth model of Prousevitich et al. (1993), which accounts for finite separation between bubbles, was further developed and used to simulate bubble growth.

The good agreement between experimental data, numerical simulation, and analytical solutions enables accurate and reliable examination of bubble growth from a limited volume of supersaturated melt. At modest supersaturations bubble growth in hydrated silicic melts (3–6 wt% water, viscosity 10^4 – 10^6 Pa·s) is diffusion controlled. Water diffusion is fast enough to maintain steady-state concentration gradient in the melt. Viscous resistance is important only at the very early stage of growth ($t < 1$ s). Under the above conditions growth is nearly parabolic, $R^2 = 2Dt\rho_m(C_0 - C_f)/\rho_g$ until the bubble approaches its final size. In melts with low water content, viscosity is higher and maintains pressure gradients in the melt. Growth may be delayed for longer times, comparable to time scales of melt ascent

during eruptions. At high levels of supersaturation, advection of hydrated melt towards the growing bubble becomes significant.

Our results indicate that equilibrium degassing is a good approximation for modeling vesiculation in melts with high water concentrations ($C_0 > 3$ wt%) in the region above the nucleation level. When the melt accelerates and water content decreases, equilibrium can no longer be maintained between bubbles and melt. Supersaturation develops in melt pockets away from bubbles and new bubbles may nucleate. Further acceleration and increase in viscosity cause buildup of internal pressure in the bubbles and may eventually lead to fragmentation of the melt.

Introduction

The expansion of volatiles exsolved from magma is the major driving force of explosive volcanic eruptions. This process begins with nucleation of bubbles in a supersaturated melt, continues with growth of these bubbles by mass transfer of volatiles and by expansion in response to the release of confining pressure during ascent, and culminates with the rupture of the thin, viscous walls between bubbles and the fragmentation of the melt to ash and pumice. The process is complex and involves a variation in many parameters. Some important ones, e.g., pressure, velocity, and viscosity, vary over a few orders of magnitude. Thus, it is useful to study each stage of the process separately, under conditions where the major controlling parameters can be isolated and examined individually.

Here we concentrate on the relatively simple case of bubble growth from a supersaturated melt, at constant pressure and temperature. Under these conditions, growth is controlled by two processes: diffusion of water molecules from the bulk of the melt towards and through the bubble–melt interface and expansion of the bubble by viscous deformation of the surrounding melt. The time scale for diffusion is $t_d = R^2/D$ and for viscous

Editorial responsibility: M. R. Carroll

Vladimir Lyakhovsky (✉) · Shaul Hurwitz · Oded Navon
Institute of Earth Sciences, Hebrew University,
I-91904 Jerusalem, Israel
Fax: + 972-2-662581
E-mail: oded@vms.huji.ac.il

deformation $t_v = \eta/\Delta P$ (see Notation List). The ratio between these characteristic time scales is the non-dimensional Peclet number that indicates which process controls the actual rate of the bubble growth:

$$Pe = \frac{t_d}{t_v} = \frac{\Delta P R^2}{\eta D}$$

Most of the industrial literature deals with cases of Peclet numbers much larger than unity, where growth rate is controlled by characteristic diffusion time scale. Epstein and Plesset (1950) developed a model of diffusional growth of bubbles in water. They considered the effect of surface tension and demonstrated that after a short time growth is parabolic (\sqrt{t}). Scriven (1959) formulated equations for phase growth in an infinite medium and simplified them to describe growth controlled by heat and mass transfer. Readey and Cooper (1966) also accounted for the role of variable melt density. Cable and Evans (1967) and Szekely and Fang (1973) examined the early stages in which growth is not parabolic. Zak and Weinberg (1980a,b) studied the simultaneous growth of many bubbles. In the geological literature, the benchmark study of Sparks (1978) reviewed early models and used the equations of Scriven (1959) to describe bubble growth in silicic melts. He noted, however, that viscous resistance could be important in hindering bubble growth in silicic melts when viscosity exceeds 10^7 Pa s. The case of high Peclet numbers was also discussed by Bottinga and Javoy (1990) in their study of bubble growth in basalts. Toramaru (1989) and Mangan et al. (1993) also assumed a parabolic growth law to calculate rates of bubble growth in a variety of silicate melts. The subject has been reviewed by Jaupt and Tait (1990) and Sparks et al. (1994).

However, in highly viscous, silicic systems, the Peclet number is small and diffusion is fast enough to approach steady state during the time it takes for the bubble to expand. A mathematical model for the intermediate case ($Pe \approx 1$) was presented by Proussevitch et al. (1993). They accounted for the viscous resistance of the melt, emphasized the role of advective flux of a volatile-bearing melt towards the growing bubble, and considered the effect of neighboring bubbles. The numerical results they obtained using this model indicated that during the initial stages, growth rate is very slow. This "delay time" was initially attributed to the effect of surface tension (Proussevitch et al. 1993), but as shown later, surface tension delays growth by no more than a fraction of a second, whereas longer delay times are due to viscous resistance of the melt during the initial stages of growth (Sparks 1994; Sahagian et al. 1994).

In contrast to the extensive theoretical modeling, the only experimental investigation of bubble growth in natural silicate melts was carried out by Murase and McBirney (1973). They investigated the growth rate of bubbles at 1 atm in rhyolitic, andesitic, and basaltic glasses of low volatile content.

We investigated the systematics of bubble growth by mass transfer of water in rhyolitic melts with high initial water contents at high pressures and temperatures. We used a model similar to that of Proussevitch et al. (1993) to simulate bubble growth when the Peclet number is approximately unity. In the case of small Peclet numbers, the model was significantly simplified by an analytical solution for the concentration profile of water in the melt. We also derived asymptotic analytical solutions that allow a better understanding of the role of the various physical parameters. The experiments conducted by Hurwitz and Navon (1994) documented the growth of water bubbles from a finite volume of rhyolitic magma under controlled conditions. A more precise measurement of the average bubble radius enabled us to test the theoretical model, to constrain important controlling parameters (e.g., diffusion coefficient and bubble separation), and to report the first experimental verification of the theory of bubble growth in silicic magma under conditions that are relevant for the early stages of magma degassing in nature.

Experimental methods and results

The data for this study were derived from the experiments performed by Hurwitz and Navon (1994) in their study of nucleation. A detailed description of the experiments can be found there. Briefly, the experiments involved hydration of small chips of rhyolitic obsidian at 150 MPa (water content of 5.3 and 5.5 wt% at 850 and 800 °C, respectively), followed by a drop of pressure, which allowed bubbles to nucleate and grow under a lower constant pressure for periods of a few seconds to a few hours. Growth time was measured from the moment stable pressure was established (3–5 s for $\Delta P < 50$ MPa; 5–10 s for larger pressure drops). This may have induced a systematic error of a few seconds, mainly in experiments where pressure drop was large and growth time was short. At the end of the growth period, samples were quenched rapidly by dropping them to the water-cooled zone of the pressure vessel. Quenching time was less than 2 s. Considering the high viscosity of the melt, negligible changes in the volume of the bubbles were expected, i.e., less than 5% change in bubble size, based on numerical simulation and heating stage experiments, where the relative volumes of the gas and liquid remained constant, until decrystallization at 300 °C.

Bubble diameter was measured in thick sections of the run products using the internal scale bar of a Nikon petrographic microscope, or after transmitting the microscopic image to a computer. Bubble-size distribution was determined by measuring the radii of 30–90 bubbles per sample, or of all bubbles where the total number of bubbles in the sample was less than 30. Bubbles close to the sample margins were avoided.

The number density of bubbles (N_d -number of bubbles per cm^3 of glass) was determined directly under

the microscope. In samples with low-number density the total number of bubbles was divided by the total volume of the sample. For higher densities bubbles were counted throughout the thickness of the sample, but only in an area exposed to the microscope with $\times 40$ objective lens (exposed area 0.07 mm^2). In highly vesiculated samples, only bubbles exposed on the surface were counted and the surface distribution was converted into a three-dimensional number density. Errors in the number density of bubbles may be as large as a

factor of two. The main source of error is the uneven distribution of bubbles. The average separation between bubbles ($2S$) for spherical geometry was deduced from the bubble number density, $1/N_d = 4\pi S^3/3$.

The number density of bubbles in each individual sample (Table 1) is strongly dependent on the availability of oxide microlites which serve as efficient nucleation sites (Hurwitz and Navon 1994). This dependence leads to variations of up to two orders of magnitude in the separation between bubbles. In the presence of ox-

Table 1 Experimental results

Sample No.	T (°C)	P _r (MPa)	t (s)	N ^c	R (μm)	SD (%)	S ^d (μm)
LGB-10	780	50	1800	78	17	12	25
LGB-17	780	100	1200	39	18	15	49
LGB-24	780	100	60	70	7	18	13
LGB-35 ^b	780	145	45	90	2	28	23
LGB-52	780	120	30	81	10	26	35
LGB-58 ^b	780	120	300	90	3	15	35
LGB-89	780	145	180	62	5	30	36
LGB-97	780	120	45	56	7	19	38
LGB-98 ^b	780	140	180	70	4	32	29
LGB-104	780	120	30	16	10	8	76
LGB-124 ^b	780	120	5	68	6	35	31
LGB-59	790	120	480	19	32	11	122
LGB-7 ^a	800	50	14400	6	125		194
LGB-16	800	50	900	10	135	19	228
LGB-18	800	100	300	17	91	21	189
LGB-39	800	120	120	21	22	8	415
LGB-53	800	120	1140	59	80	17	329
LGB-55	800	112	30	53	11	9	492
LGB-57	800	120	180	22	27	13	319
LGB-84	800	135	180	8	14	5	492
LGB-85	800	80	180	32	56	12	228
LGB-88	800	16	5	43	18	27	92
LGB-101	800	25	30	30	71	7	81
LGB-102 ^a	800	42	30	14	22		35
LGB-135	800	120	60	43	13	10	92
LGB-136	800	120	80	5	17	4	683
LGB-74	850	120	10800	6	90	19	852
LGB-76	850	120	180	40	25	8	349
LGB-81	850	100	180	20	35	5	355
LGB-82	850	40	180	7	52	16	71
LGB-95	850	15	30	6	164	6	199
LGB-111	850	30	60	21	46	13	62
LGB-114	850	50	180	30	71	9	88
LGB-115	850	60	180	22	63	9	106
LGB-116	850	35	60	20	86	7	192
LGB-117 ^a	850	44	180	17	24		30
LGB-118	850	62	180	35	38	16	58
LGB-119	850	35	120	25	51	24	68
LGB-120	850	36	15	25	37	13	158
LGB-121 ^a	850	36	90	15	22		29
LGB-122	850	35	5	25	40	9	147
LGB-123 ^a	850	30	30	14	70		88
LGB-125	850	50	7	38	20	6	100
LGB-126	850	50	6	35	19	10	65
LGB-127	850	70	6	42	8	16	43
LGB-128	850	50	60	7	63	13	131
LGB-129	850	50	60	24	38	9	75
LGB-130	850	70	60	44	16	12	29

Note: The table includes three new experiments (LGB-130, 135, 136) not reported by Hurwitz and Navon (1994), new determination of R, three new estimations of S (LGB-58, 126, 129), and one correction in t (LGB-128)

^a Bubble size and separation were counted only on the surface of the sample (see text)

^b Bimodal bubble distribution

^c N number of bubbles included in calculation of R and its standard deviation

^d $S = (3/(4\pi N_d))^{1/3}$ (see text for details)

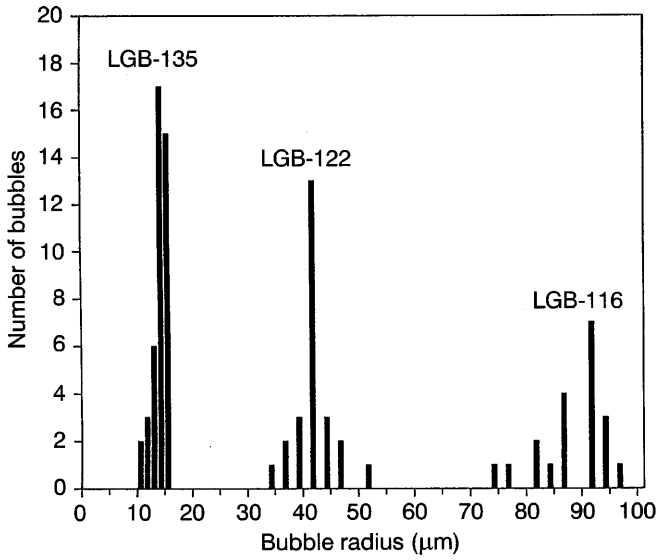


Fig. 1 Bubble-size distribution for representative samples

ides (temperature lower than 800 °C) nucleation was intensive, and the typical separation between bubbles was less than 50 μm. In samples where no oxides were present, pressure drops of less than 80 MPa ($\Delta P < 80$ MPa) led to limited nucleation and large separation between bubbles (92–852 μm). In experiments where ΔP exceeded 80 MPa, nucleation was intensive, and, even in the absence of microlites, bubble separation became smaller (29–228 μm).

Figure 1 presents the bubble-size distribution in representative samples. The range of bubble sizes in individual samples is always narrow, and does not exceed a factor of two. In most cases the standard deviation from the average radius is less than 20%. In some samples bimodal distribution was observed, with a few large bubbles and many small ones. The small bubbles nucleated in response to the controlled pressure drop. The large bubbles that grew during the hydration period, probably in response to small fluctuations in pressure, were ignored (Hurwitz and Navon 1994).

Some general correlations were observed in the raw data. For example, the average radius of samples held at 120 MPa grows with increasing time, and the radius in experiments where separation was large fit the model of Scriven (1959). However, as was quickly realized, in order to fully interpret the experimental data set, a more elaborate model was required.

Mathematical model

The model presented here is based on the physical model suggested by Prousevitch et al. (1993). Briefly, each bubble gets water from a spherical shell of melt with initial radius S_0 . The mass of the melt in the shell is conserved during growth, as is the total amount of water in the bubble + shell.

The governing equations

Following is a brief description of the main model equations from Prousevitch et al. (1993), together with our simplifications for small Peclet numbers. Volatile mass transfer expressed by Fick's law of diffusion for spherical symmetry is of the form:

$$\frac{\partial C}{\partial t} + v_r \frac{\partial C}{\partial r} = \frac{1}{r^2} \frac{\partial}{\partial r} \left(D r^2 \frac{\partial C}{\partial r} \right) \quad (1)$$

When $Pe \approx 1$ or $Pe > 1$, Eq. (1) is solved in its original form, including temporal derivation of the concentration and the advection term (dynamic model). For $Pe < 1$ these two terms may be neglected, leading to a quasi-static approximation, where the concentration of water is described by the steady-state diffusion equation:

$$\frac{1}{r^2} \frac{\partial}{\partial r} \left(D r^2 \frac{\partial C}{\partial r} \right) = 0 \quad (1a)$$

This reduction enables a significant simplification of the mathematical procedure and enables deriving an asymptotic analytical solution for the growth law (Appendix A).

Two boundary conditions are necessary for solving the above equation. The first, at the bubble–melt interface, is derived from the equilibrium between dissolved water in the melt and the gas in the bubble. This is approximated using a Henry's law solubility model for water in rhyolitic melts (Burnham 1975):

$$C_R = K_h \cdot \sqrt{P_g} \quad (2)$$

The second boundary condition, at $r=S$, is derived from the condition of water mass conservation in the spherical shell of melt that surrounds the bubble:

$$\frac{4}{3} \pi \rho_g R^3 + \int_R^S 4 \pi r^2 \rho_m C(r) dr = \frac{4}{3} \pi S_0^3 C_0 \rho_m \quad (3)$$

Equation (3) also defines the final bubble radius that is reached when the concentration gradient of water in the melt becomes zero. Substitution of the equilibrium water concentration ($C = C_f$) into Eq. (3) and integration yields:

$$R_f^3 = S_0^3 (C_0 - C_f) \frac{\rho_m}{\rho_g} \quad (3a)$$

The viscous deformation of the surrounding melt is described by the continuity and momentum equations. Melt density varies slightly with water content, but to a good approximation, $\rho_m = \text{const}$ and the continuity equation describing the velocity field in the melt surrounding a bubble with growth rate V_R (Prousevitch et al. 1993) is simply:

$$v_r(r) = V_R R^2 \frac{1}{r^2} \quad (4)$$

The relations between the gas pressure in a bubble, confining pressure, surface tension effects, and viscous

resistance of the melt are described by the Navier-Stokes equation. For an incompressible Newtonian melt with constant viscosity, low Reynolds number ($Re = \rho V_R S / \eta \ll 1$) and constant final pressure, the mechanical behavior of the bubble-melt system given by Prousevitch et al. (1993) is:

$$P_g - P_f = \frac{2\sigma}{R} + 4\eta V_R \left(\frac{1}{R} - \frac{R^2}{S^3} \right) \quad (5)$$

The omission of the acceleration term is justified because of the low Reynolds number. When the bubble is at its critical size, it is in metastable mechanical and chemical equilibrium with the melt. The internal pressure defined by Henry's law (Eq. (2)) is fully compensated by the surface tension and $V_R = 0$. Under these conditions, Eq. (5) yields:

$$R_{CR} = \frac{2\sigma}{\frac{C_0^2}{K_h^2} - P_f} \quad (5a)$$

The last equation required for modeling bubble growth defines volatile mass balance at the bubble-melt interface:

$$\frac{dm}{dt} = \int D \rho_m \frac{\partial C}{\partial r} d\gamma \quad (6)$$

where γ is a surface element. To simulate bubble growth under constant pressure we solve the diffusion equation, either in its complete form (Eq. (1)) or in the reduced form for low Peclet numbers (Eq. (1a)), using boundary conditions defined in Eqs. (2) and (3), and melt velocities of Eq. (4). Finally, Eq. (5) is solved for the bubble growth rate, V_R . The resulting concentration gradient is then used to solve Eq. (6), from which the new gas density and pressure can be calculated, assuming ideal behavior.

Dynamic case

For the dynamic case ($Pe \approx 1$) the boundary condition defined by Eq. (3) which expresses mass conservation of the melt may be simplified. Differentiation with respect to time yields:

$$\frac{d}{dt} \left(\frac{4}{3} \pi \rho_g R^3 \right) + \frac{d}{dt} \int_R^S 4 \pi r^2 \rho_m C(r) dr = 0 \quad (7)$$

Substituting the temporal derivation of water concentration from Eq. (1) into Eq. (7) and integrating we obtain:

$$\frac{d}{dt} \left(\frac{4}{3} \pi \rho_g R^3 \right) + 4\pi S^2 \rho_m D \left(\frac{\partial C}{\partial r} \right)_S - 4\pi R^2 \rho_m D \left(\frac{\partial C}{\partial r} \right)_R = 0 \quad (8)$$

Using the mass-balance equation (Eq. (6)), Eq. (8) may be separated into two conditions used by Prouse-

vitch et al. (1993). The first is identical to the mass-balance equation (Eq. (6)) and expresses accumulation of mass in the bubble by diffusion:

$$\frac{d}{dt} \left(\frac{4}{3} \pi \rho_g R^3 \right) = 4\pi R^2 \rho_m D \left(\frac{\partial C}{\partial r} \right)_R \quad (9)$$

Combining Eqs. (8) and (9) yields the second boundary condition for $r=S$, which corresponds to mass conservation of water within the shell:

$$\left(\frac{\partial C}{\partial r} \right)_S = 0 \quad (10)$$

A numerical procedure for modeling bubble growth in the dynamic case is described in Appendix B.

Quasi-static case

The quasi-static approximation was developed for the case of $Pe < 1$, where the temporal derivation of concentration, and the advection term in the diffusion equation, may be neglected. The major advantage of this approximation is that it leads to a general solution for the distribution of volatile concentration around the growing bubble:

$$C(r) = A - \frac{B}{r} \quad (11)$$

and to analytical solutions for the constants A and B. Combining Eqs. (11) and (3) and integrating yields:

$$\begin{aligned} \frac{4}{3} \pi \rho_g R^3 + \frac{4}{3} \pi \rho_m (S^3 - R^3) A - 2\pi \rho_m (S^2 - R^2) B \\ = \frac{4}{3} \pi \rho_m S_0^3 C_0 \end{aligned}$$

Combining this equation with Eq. (2) together with the condition for conservation of melt volume ($S^3 - R^3 = S_0^3$), we can calculate the values of constants A and B:

$$A = C_R + \frac{B}{R} \quad (12)$$

$$B = \frac{S_0^3 (C_0 - C_R) - \frac{\rho_g}{\rho_m} R^3}{\frac{S_0^3}{R} - \frac{3}{2} (S^2 - R^2)} \quad (12a)$$

For further simulation we need only the concentration gradient on the bubble-melt interface, which is of the form:

$$\left(\frac{\partial C}{\partial r} \right)_R = \frac{B}{R^2} = \frac{S_0^3 (C_0 - C_R) - \frac{\rho_g}{\rho_m} R^3}{S_0^3 R - \frac{3}{2} (S^2 - R^2) R^2} \quad (13)$$

This simplification leads to a significant reduction in the numerical calculations for small Peclet numbers

(Appendix B). More importantly, an analytical asymptotic solution of the model equations for $t \rightarrow \infty$ can be derived. For this solution we assume infinite bubble separation ($S \gg R$) and neglect the surface tension ($R \gg R_{cr}$). The first two terms of the asymptotic solution are:

$$R^2 = \frac{2D\rho_m(C_0 - C_f)}{\rho_g} t - \frac{2}{3} \frac{D\eta}{P_f} \frac{\rho_m}{\rho_g} (2C_0 + C_f) \log\left(\frac{\Delta P}{\eta} t\right) \quad (14)$$

Further terms, of the order of $1/t$, $1/t^2$, and smaller, are negligible (Appendix A).

It is interesting that although for low Peclet numbers the dominant time scale is that of viscous response (t_v) and the temporal derivation of the concentration in the diffusion equation was neglected (Eq. (1a)), for a relatively long period, the growth law retains the same parabolic form as common diffusion controlled processes, and is independent of viscosity. The effective diffusion coefficient is:

$$D_{eff} = \frac{2D\rho_m(C_0 - C_f)}{\rho_g} \quad (15)$$

and its value depends on the diffusion coefficient of water, initial water content, and the final confining pressure. Figure 2 compares the analytical solution and the full numerical calculation for the same parameters. At modest supersaturation the numerical solution quickly approaches the asymptotic value predicted by Eq. (15).

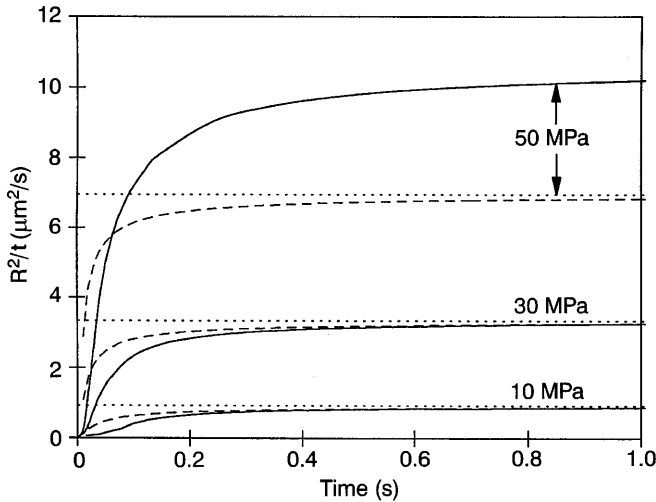


Fig. 2 The effective diffusivity (R^2/t) for ΔP of 10, 30, and 50 MPa, $\eta = 5 \times 10^4$ Pa s, and $S \gg R$. *Dotted lines* indicate the value of the asymptotic solution after a long time (Eq. 15); *dashed lines* indicate the first and the second terms of the asymptotic solution (Eq. (14)); *solid lines* indicate results of numerical calculations. The quasi-static solution was used for all times at $\Delta P = 10$ or 30 MPa. At $\Delta P = 50$ MPa, the quasi-static solution was used until the Peclet number exceeded 0.01 at $t = 0.02$ s. The dynamic solution was used at later times. The deviation of the asymptotic approximation from the numerical solution at $\Delta P = 50$ MPa is due to the growing importance of advective flux, neglected in the former

Equation (14) yields an even better approximation and deviates only at very short times, when additional terms are still important. We note that an approximate solution for growth of bubbles from finite volume of melt may be obtained by replacing the gradient for the single-bubble case by Eq. (13). At high supersaturations ($P_f < 110$ MPa, for the parameters of Fig. 2), advection becomes important, the analytical solution may not be used, and the quasi-static solution must be replaced by the dynamic one as the bubble grows and Pe exceeds 0.01.

Model parameters and results of numerical simulation

The numerical code developed was used for simulating bubble growth under conditions corresponding to all the experiments listed in Table 1. Input parameters include the experimentally controlled, initial water content (C_0), confining pressure (P_f), temperature (T) and run duration, calculated bubble separation, and predetermined parameters, as discussed below. The model output parameter was the bubble radius corresponding to the input parameters of each experiment.

Initial bubble separation was calculated from the number density of bubbles, and the observed radius, ($S_0^3 = S_f^3 - R_f^3 = 3/4 \pi N_d - R_f^3$). Gas densities were calculated using the ideal gas law. Comparison to more realistic densities calculated using the modified Redlich-Kwong equation of state (Holloway 1977) demonstrates that deviations are less than 14% in volume and less than 5% in bubble radius. Measured initial water contents of 5.5 and 5.3 wt% (at 800° and 850°C, respectively; Hurwitz and Navon 1994) correspond to Henry's constants of 4.49×10^{-6} and 4.33×10^{-6} Pa $^{-0.5}$, slightly higher than the commonly used value of 4.11×10^{-6} Pa $^{-0.5}$ (Burnham 1975), but in good agreement with the experimental data of Silver et al. (1990). Melt density of 2300 kg/m 3 at 5.3 wt% water was compiled from the data of Silver et al. (1990).

The surface tension used in the simulation ($\sigma = 0.06$ N/m) is that estimated by Hurwitz and Navon (1994) based on the experimental results of Epel'baum et al. (1973). It varies with water content up to a maximum value of 0.2 N/m in dry rhyolite at 850°C (Murase and McBirney 1973). The value used for melt viscosity, 5×10^4 Pa s, is approximately higher by a factor of two than the values obtained from Shaw (1972), or Baker and Vaillancourt (1995), but is in agreement with Persikov (1991). This presumably higher value compensates, at least in part, for the increase in viscosity, because the water content of the melt drops during the growth period. The diffusion coefficient of water in highly hydrated rhyolitic melts is not well constrained, due mainly to the variation with varying water content. We used a subset of our data to constrain the diffusion coefficient of water to $2-3 \times 10^{-11}$ m 2 /s (see below).

Surface tension, viscosity, and diffusion coefficient of water are not well constrained, either due to lack of

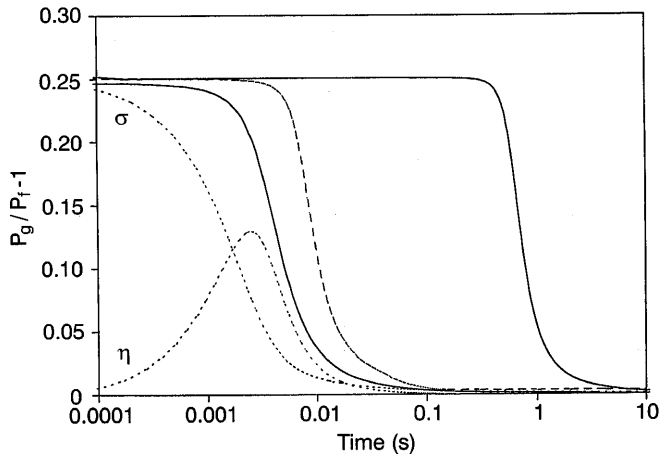


Fig. 3 The effect of viscosity and surface tension on the growth regime of bubbles. The normalized excess pressure in the bubbles (P_g/P_r-1) is plotted as a function of time. Initial conditions are $P_r=120$ MPa, $\Delta P=30$ MPa, $D=2 \times 10^{-11}$ m²/s, $\sigma=0.05$ N/m, $\eta=10^4$ Pa s. The contribution of surface tension (σ) to the excess pressure quickly falls after 0.001 s. The viscosity term (η) also decays after 0.01 s. Their combined effect is shown by the *left solid line*. The *dashed line* shows the effect of increasing surface tension to 0.2 N/m (its value in dry rhyolite). The *solid line* on the right corresponds to viscosity of 10^6 Pa s, where growth is delayed by approximately 1 s

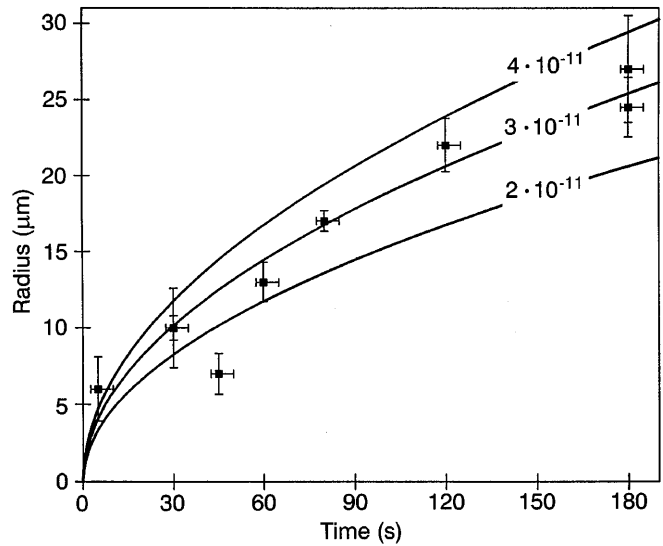


Fig. 4 Bubble radius as a function of growth time. *Triangles* indicate experimental results for samples decompressed to 120 MPa and where $R \ll S$. *Solid lines* indicate simulation of growth under the above conditions, using $\eta=5 \times 10^4$ Pa s different values of diffusion coefficient ($D=2, 3,$ and 4×10^{-11} m²/s). Error bars indicate the standard deviation from the average radius, and the time it takes for the pressure to stabilize

data or because all three vary with the water content of the melt. Figure 3 shows the sensitivity of the solution to variations in melt viscosity and surface tension. Both parameters act against the expansion of the bubble and inhibit the fall of internal pressure. Surface tension is only important at very early stages, when the bubble radius is close to the critical value and its effect falls as $1/r$. At $\Delta P=30$ MPa it is negligible after 0.01 s for $\sigma=0.05$ N/m and after 0.1 s for the surface tension of dry rhyolite, $\sigma=0.2$ N/m.

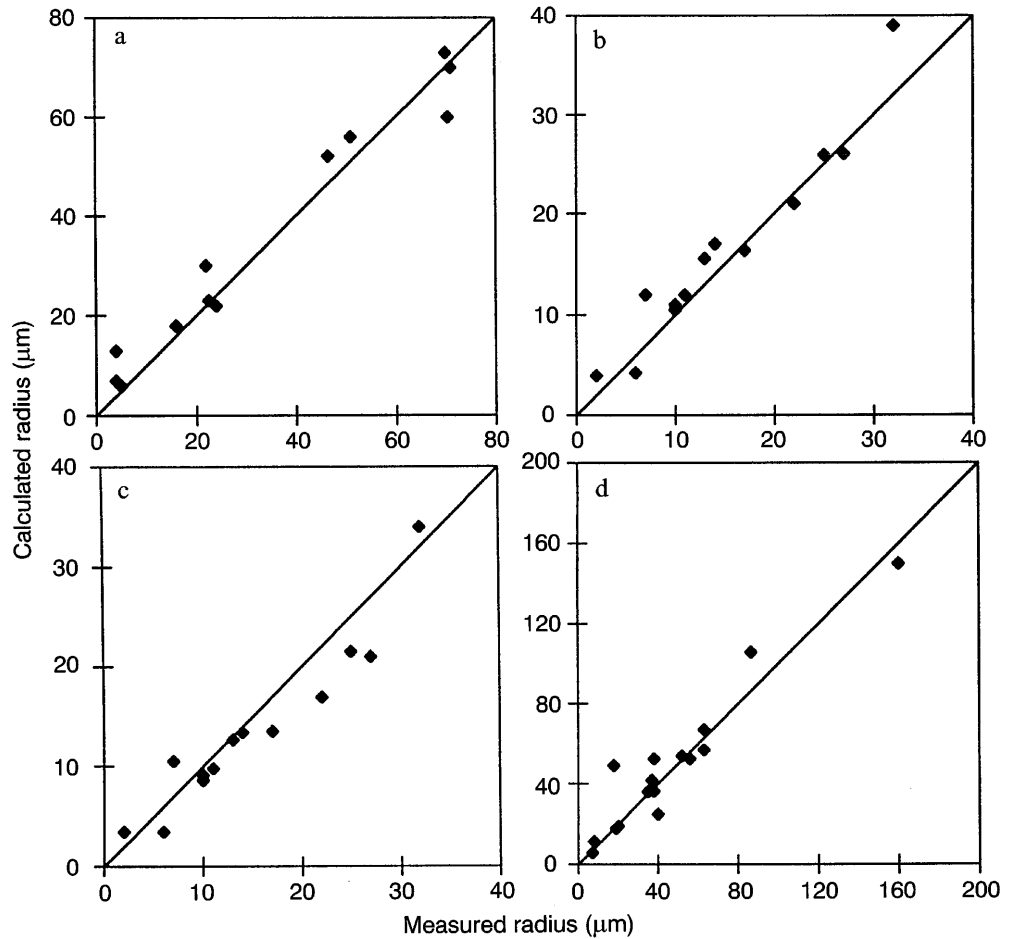
Viscosity is important when the ratio of radial growth velocity to bubble radius, V_R/R , is high. At early stages of growth, when bubble size is close to critical, the bubble is close to mechanical equilibrium and the radial growth velocity is low. Later, melt velocity reaches a maximum value and then declines when the radius is large and grows slowly with increasing volume. At this stage the viscous resistance is small and $P_g \approx P_r$. When $\eta=10^4$ Pa s the viscous resistance of the melt decays quickly and may be neglected after 0.01 s. However, at $\eta > 10^6$ Pa s the delay induced by the viscous resistance of the melt is important for times of 1 s or more and must be considered. The role of viscosity and surface tension in delaying bubble growth has been discussed by Sparks (1994) and Sahagian et al. (1994). Our numerical code allows simulation of the very early stages of growth. Moreover, the analytical solution derived (Eq. (14)) enables direct examination of the role of viscosity and diffusivity during these stages when separation is still large and the Peclet number is small. Because viscosity appears only in the second term of Eq. (14), which depends on $\log(t)$, its effect disappears

quickly. This can be seen in Fig. 2, in which the numerical and analytical solutions both show that the effect of viscosity dies after approximately 0.2 s (for $\eta=5 \times 10^4$ Pa s). At later times the bubbles behave as if they grew in accordance with the parabolic growth law (Eq. (15)) from $t=0$.

As noted above, the diffusion of water in melts with high water contents is not well constrained by experimental data; we used a subset of our experiments to estimate its value. Figure 4 shows the average radii reached in experiments in which pressure was dropped from 150 to 120 MPa. In most runs the average separation is large compared with the final radius. Numerical simulations of the growth process were conducted assuming large separation and diffusion coefficients of $2-4 \times 10^{-11}$ m²/s. These values of D are in good accord with seven of the nine samples. Sample LGB-97 falls below the calculated curves, probably because bubbles grew in clusters around iron-oxide crystals, so that the actual separation was smaller than the average value and limited the final size. LGB-124 was quenched after a very short time, comparable to the time it took to drop and stabilize the pressure; thus, its growth time is not well constrained and is probably longer. Similar simulations with $\eta=10^6$ Pa s (not shown in graph) caused only a small shift in the calculated growth curves with most experimental points best fitted by $D=3-4 \times 10^{-11}$ m²/s; thus, it appears that the best value for the diffusion coefficient at 5 wt% water is 3×10^{-11} m²/s.

The above value falls within the large range suggested by Karsten et al. (1982) and Lapham et al.

Fig. 5a-d Comparison of average bubble radii measured in the experimental samples with the numerical results for identical conditions. **a** Samples that reached their final radius (according to the simulations). **b** Samples where bubbles grew at $P_f > 110$ MPa, compared with radii calculated using $D = 3 \times 10^{-11}$ m²/s. **c** Same as **b**, but using $D = 2 \times 10^{-11}$ m²/s. **d** Samples held at $P_f < 110$ MPa compared with numerical results calculated using $D = 2 \times 10^{-11}$ m²/s



(1984). It is higher by a factor of 4 than the value obtained by extrapolating the expression derived by Zhang et al. (1991) to high water contents and high temperatures. Zhang et al. (1991) suggested that the dependence of the bulk diffusivity of water on the total water content of the melt is due solely to varying proportions of hydroxyls and molecular water, and that the intrinsic diffusivity of molecular water is constant and does not vary with water content. The higher values we obtained may reflect an increase in the intrinsic diffusivity of molecular water with increasing water content in the melt. Clearly, more precise experiments aimed at direct measurements of diffusion profiles are needed for accurate determination of the diffusion coefficient at high water contents. However, because the experiments of Zhang et al. (1991) were limited to water content of less than 1.7% and temperatures of less than 550 °C, the value obtained here appears to be the best currently available coefficient for melts with high water content.

All the experiments were simulated using the parameters discussed above and water diffusivities of $2\text{--}3 \times 10^{-11}$ m²/s. A lower value of 2×10^{-11} m²/s was used in simulations of bubble growth at low pressures in order to compensate for the decrease in diffusivity with water content. The measured and calculated radii are compared in Fig. 5. This simple presentation enables

comparing the results for runs of different duration, final pressures, and bubble number densities. In 11 cases simulations indicated that bubbles closely approached their final radii, either because the separation between bubbles was small, or because run durations were long. In these cases bubble radii are governed by a simple mass balance (Eq. (3a)). The close fit we found between measured radii and the simple mass balance calculation (Fig. 5a) is a good indication that average radii measured in the samples are representative of bubble radii in the melt at the end of the growth period, and that shrinkage during quenching is small. It also ascertains that the random spatial distribution of bubbles can be adequately modeled by a regular geometry with an average separation.

The success of the model in simulating the dynamics of bubble growth is evident in Fig. 5b, c, and d, which compares the bubble size in runs where the bubbles did not attain their final, equilibrium size. The results for runs where pressure drop was modest ($\Delta P < 40$ MPa) are shown in Fig. 5b and c. Under these conditions the advective flux is negligible and the bubbles grow mainly by diffusive mass transfer. A diffusion coefficient of 3×10^{-11} m²/s slightly overestimates bubble radii, but yields a closer fit than $D = 2 \times 10^{-11}$ m²/s. The data for bubbles that grew after large pressure drops ($\Delta P > 40$ MPa; Fig. 5d) are better fitted by

$D=2 \times 10^{-11} \text{ m}^2/\text{s}$, probably because of the lower water concentrations in the melt surrounding the bubbles.

The good agreement between the experimental data and the numerical simulation reinforces in the applicability of the physical model, the numerical code, and the melt properties used in the simulations.

Discussion

The experiments reported herein provide the first comprehensive data set on the dynamics of bubble growth in natural silicate melts at pressures, temperatures, and water contents corresponding to the early stages of natural volcanic eruptions. In these experiments bubbles grew under constant confining pressure. Although it is unlike the natural situation where pressure decreases continuously, this design has some important advantages. Nucleation took place in a single, short event upon the drop of pressure, so that growth time is well defined and bubble-size distribution is well represented by the average radius. In addition, the experimental results can be compared with existing models (Scriven 1959; Sparks 1978; Proussevitch et al. 1993).

Using the physical model of Proussevitch et al. (1993) and our improved numerical code, we were able to closely fit the experimental results within a wide range of supersaturation pressures, bubble separation, and growth time. We also derived an asymptotic analytical solution describing the growth of bubbles under conditions where the Peclet number ($\Delta P R^2 / \eta D$) is small and $R \ll S$. This solution enables clearly understanding the relative roles of supersaturation, confining pressure, viscosity, and diffusivity. The good agreement between experiments, analytical solution, and numerical simulations demonstrates the validity of the model and allows us to assess the accuracy of current models and the role of the various parameters.

The approximate parabolic growth law derived by Sparks et al. (1994; their Eq. (13)) is similar in form to the asymptotic solution we derived (Eq. (15)), but is larger by a factor of three. The reason for the discrepancy is the unrealistic concentration gradient assumed by these authors. This discrepancy is eliminated if the steady-state gradient, $(C_0 - C_f)/R$ (our Eq. (13), with $S \approx S_0 \gg R$), is used instead. An equation identical to Eq. (15) can be derived using Scriven's (1959) model for the case of high Peclet numbers.

Figure 6 compares the results of the present numerical model with the predictions of the growth model of solitary bubbles formulated by Scriven (1959) and used by Sparks (1978). Calculating R/\sqrt{t} as a function of P_f for solitary bubbles ($S \gg R$) and using melt parameters appropriate for our experiments yields a curve that envelopes the experimental data and is in excellent agreement with Scriven's model. The differences are due mainly to the limitations of the polynomial approximation of the growth constant, β , needed for Scriven's so-

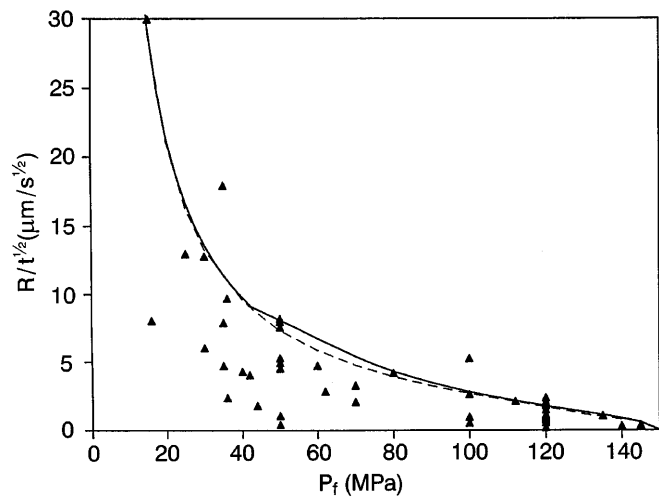


Fig. 6 The effect of confining pressure on the parabolic growth rate of bubbles. *Triangles* indicate experimental results. *Solid line* indicates Scriven's growth model for solitary bubbles using the polynomials given by Sparks (1978) and $D=2 \times 10^{-11} \text{ m}^2/\text{s}$. *Dashed line* indicates results of numerical calculations, using $S \gg R$, $\eta=5 \times 10^4 \text{ Pa s}$, and $D=2 \times 10^{-11} \text{ m}^2/\text{s}$ (see discussion in text)

lution (Sparks 1978). This good fit is expected because viscosity in our experiments was small and P_g quickly reached the constant value of P_f . At higher viscosity Scriven's model is not valid and description of the viscous effect, as given in the model used here, is required.

Most experimental results fall below the line which plots the growth of solitary bubbles and can be simulated only by models that account for finite separation between bubbles. In this case the amount of water available for each bubble is limited, and it cannot grow beyond a finite size: $(R_f^3 = S_0^3 \rho_m (C_0 - K_h \sqrt{P_f}) GT / MP_f)$. In fact, the radius of LGB-18 (91 μm), the only sample which falls much above the solitary bubble line, is within error of the calculated final radius (88 μm). This leads us to conclude that the growth time recorded for this run is most probably erroneous and was actually longer than 300 s.

The effect of separation, along with that of initial water content and the associated viscosity and diffusivity, are demonstrated in Fig. 7. We examine two typical situations. The dashed line follows bubble growth at $P_f=120 \text{ MPa}$ from a melt with initial water content of 5.3 wt% water, corresponding to a supersaturation pressure of 30 MPa. If initial separation between bubbles is 50 μm ($N_d=2 \times 10^6$ bubbles per cubic centimeter), it takes approximately 60 s to reach 90% of the final radius of 19 μm . If the number of bubbles increases to 2.5×10^8 ($S_0=10 \mu\text{m}$), then only 3 s are required to approach the final radius of 3.8 μm .

During eruption, melt emerging from the magma chamber first ascends at low velocity and accelerates when it approaches the fragmentation level (c.f. Fig. 15 of Sparks et al. 1994). Typical velocities at the early

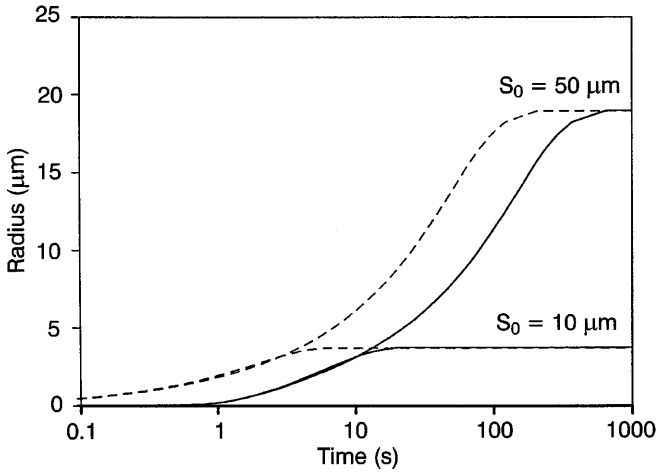


Fig. 7 The evolution of bubble radius with time for samples with different water content. *Dashed lines* indicate bubbles growing from a melt with initial water concentration of 5.3 wt% at 120 MPa ($D=3 \times 10^{-11} \text{ m}^2/\text{s}$, $\eta=5 \times 10^4 \text{ Pa s}$). *Upper line* indicates bubbles growing from spherical shells of initial thickness 50 μm ; *lower line* indicates shell of thickness 10 μm . *Solid lines* indicate same, for a melt with initial water content of 3 wt% at 43 MPa ($D=1 \times 10^{-11} \text{ m}^2/\text{s}$, $\eta=5 \times 10^6 \text{ Pa s}$). Pressures were chosen so that in both cases bubbles growing from shells of similar thickness reach the same final radius of 19 μm (for $S_0=50 \mu\text{m}$), or 3.8 μm (for $S_0=10 \mu\text{m}$). Note that growth is nearly parabolic, but is distorted because of the logarithmic scale for the time axis

stage are of the order of a few kilometers per hour (Sparks et al. 1994; Klug and Cashman 1994). At these rates it takes a few hundred seconds for the pressure to decrease by 30 MPa. If $N_d > 10^6 \text{ cm}^{-3}$, bubbles have enough time to reach their final size. During ascent melt and bubbles are in equilibrium and no further nucleation is expected. Under these conditions magma density follows the equilibrium condition: $\rho = \rho_m (1 + (C_0 - C_R) \rho_m / \rho_g)^{-1}$. Such equilibrium is commonly assumed in many models of magma degassing (Wilson et al. 1980; Jaupart and Allegre 1991; Papale and Dobran 1993). As the magma approaches the fragmentation level, the pressure is lower (50 MPa in the example given in Fig. 7), the water content of the melt is only 3 wt%, the viscosity is higher by two orders of magnitude, and the diffusion coefficient of water is lower by a factor of three (Chekhmir et al 1989). In addition, ascent velocities are high and a pressure decrease of approximately 6 MPa occurs in less than 10 s. (This drop of pressure was chosen to produce bubbles of the same final radius as in the 30 MPa decrease from 150 to 120 MPa). The shorter time scale and the slower response of the melt prevent complete equilibrium, and supersaturation develops in melt regions which are not close to existing bubbles and may induce nucleation of a new generation of bubbles (c.f. the natural samples shown in Toramaru 1990; Klug and Cashman 1994).

Figure 7 also shows the growing effect of viscosity as water content decreases. In melt with 5.3% water and viscosity of $5 \times 10^4 \text{ Pa s}$, the melt follows the parabolic growth law (the dashed line). At 3 wt% water, when

viscosity is higher and diffusion slower, growth is delayed and the bubble radius is nearly zero for approximately 1 s. This effect must grow in importance as ascent velocity increases. Confining pressure drops rapidly and internal excess pressure builds up in the bubbles. The growing pressure gradients and the increase in melt viscosity may lead to fragmentation.

Under the conditions prevailing in the experiments reported herein, the role of viscosity is limited to the very early stages of the runs. As water content of the melt decreases, viscosity increases and its role becomes significant. In order to improve our understanding of the fast degassing just before fragmentation, additional experiments aimed at examining the viscous response, as well as a model with variable pressure, viscosity, and diffusion coefficient are required.

Conclusions

The agreement between experimental data, numerical simulation, and asymptotic analytical solutions enables accurate and reliable examination of bubble growth from limited volume of supersaturated silicic melts. At low supersaturation (less than 40 MPa in the present set of experiments with $C_0 \approx 5 \text{ wt\%}$ water) growth is diffusion-controlled and can be closely approximated by an analytical solution. At higher supersaturation advection of hydrated melt towards the growing bubble becomes significant and growth should be modeled with the complete solution of the diffusion equation.

The initial water content and the final confining pressure are the important factors controlling bubble growth. Their combination defines the supersaturation that has a crucial role in determining the nucleation efficiency (Hurwitz and Navon 1994), and hence, the separation between bubbles. Through Henry's law they determine the total amount of water available for the bubbles and control the final volume fraction of gas in the melt. They also determine the gradients of concentration and pressure in the melt which surrounds the bubble, and hence, the rate of growth.

In the experiments reported herein, the most important melt property is the diffusion coefficient of water. The experimental data indicate that the diffusion coefficient at $\approx 5 \text{ wt\%}$ water is close to $3 \times 10^{-11} \text{ m}^2/\text{s}$. A coefficient of $2 \times 10^{-11} \text{ m}^2/\text{s}$ fits experiments where water content decreases to 2–4 wt%. These coefficients are three to four times higher than the values predicted by Zhang et al (1991).

Our data indicate that equilibrium degassing is a good approximation for ascending magma just above the nucleation level, where magma velocities are low and water concentrations high (a few kilometers per hour and more than 3 wt% water). When the melt accelerates and water content decreases, growth can no longer approach equilibrium, and supersaturation develops in melt pockets away from bubbles and new bubbles may nucleate. Further acceleration and in-

crease in viscosity cause a buildup of internal pressure in the bubbles and may eventually lead to fragmentation of the melt.

Acknowledgements We thank Anatoly Chekhir for many useful discussions, Steve Sparks for his critical advice, and Mike Carroll, Janni Barclay, and Jeremy Phillips for reviewing this article. Funding was provided by the Israel–USA Binational Science Foundation. V. L. acknowledges partial support by a Golda Meir fellowship.

Appendix A

Asymptotic solution of the quasi-static approximation

We derived an analytical asymptotic solution of the quasi-static approximation of model equations for $t \rightarrow \infty$. For this solution the surface tension may be neglected ($R \gg R_{cr}$), and for simplicity we assume infinite bubble separation ($S \gg R$). All the calculations are presented in the non-dimensional form and only the final result is transformed back to the dimensional form. The main parameter governing the style of bubble growth is supersaturation pressure (ΔP), which is taken as a scale of the pressure ($\bar{p} = \Delta P$). In accordance, density can be scaled as $\bar{\rho} = \bar{p}M/GT$. The critical radius is chosen as a length scale ($\bar{R} = R_{cr}$). The velocity scale ($\bar{v} = \bar{R}/\bar{t}$) is estimated using the assumption that the characteristic pressure is proportional to the velocity gradient multiplied by the viscosity of the melt ($\bar{p} = \eta\bar{v}/\bar{R}$). Finally, the time scale is $\bar{t} = \eta/\bar{p}$. Using this scaling where all parameters are in their non-dimensional form, neglecting the effect of surface tension and mechanical interaction between bubbles, Eq. (5) transforms to:

$$p_g = p_f + 4 \frac{V_R}{R} \quad (A1)$$

The concentration gradient on the bubble–melt interface (Eq. (13)) is of the form:

$$\left(\frac{\partial C}{\partial r}\right)_R = \frac{C_0 - C_R}{R} \quad (A2)$$

Inserting Eq. (A2) into Eq. (9) and differentiation yields:

$$R^2 \frac{d\rho_g}{dt} = 3 \frac{D\eta}{\bar{R}\bar{p}} \bar{\rho}(C_0 - C_R) - 3\rho_g R V_R \quad (A3)$$

We search a solution $R(t)$, for Eqs. (A1)–(A3) in the form of a time series:

$$R = \left[a_0 t + a_1 \log t + a_2 \frac{1}{t} + \dots \right]^{1/2} \quad (A4)$$

Actually, because we are interested in the asymptotic solution for $t \rightarrow \infty$, we need to define only the zero and the first approximation of the solution: a_0 and a_1 . Using Eq. (A4) we may calculate two useful variables for the construction of the solution:

$$R \cdot V_R = \frac{1}{2} \frac{d}{dt} (R^2) = \frac{1}{2} \left(a_0 + \frac{a_1}{t} \right) + o(t^{-2}) \quad (A5)$$

$$\frac{V_R}{R} = \frac{R \cdot V_R}{R^2} = \frac{1}{2t} + o(t^{-2}) \quad (A6)$$

Inserting Eq. (A6) into Eq. (A1) yields:

$$p_g = p_f + \frac{1}{2t} + o(t^{-2}) \quad (A7)$$

Using the non-dimensional form of the ideal gas equation of state ($\rho_g = p_g$) the temporal derivation of the gas density is of the form:

$$\frac{d\rho_g}{dt} = -\frac{2}{t^2} + o(t^{-2}) \quad (A8)$$

We also use Henry's law (Eq. (2)) for expressing C_R as a function of P_g . Inserting Eq. (A7) into Eq. (2) yields:

$$C_R = K_h \sqrt{P_f} + \frac{K_h \sqrt{P_f}}{t P_f} + o(t^{-2}) \quad (A9)$$

We insert Eqs. (A4)–(A8) into Eq. (A3) and reduce it to:

$$\begin{aligned} & \frac{3}{2} a_0 P_f - 3 \frac{D\eta}{\bar{p}\bar{R}} \rho_m (C_0 - K_h \sqrt{P_f}) \\ & + \frac{1}{t} \left[a_0 + \frac{3}{2} P_f a_1 + 3 \frac{D\eta}{\bar{p}\bar{R}} \bar{\rho} \frac{K_h \sqrt{P_f}}{P_f} \right] + o(t^{-2}) = 0 \end{aligned}$$

The coefficients a_0 and a_1 can be defined and inverted into the initial form of the solution (Eq. (A4)). Back-transformation of Eq. (A4) into the dimensional form, the final asymptotic solution is:

$$\begin{aligned} R^2 = & \frac{2D\rho_m(C_0 - C_f)}{\rho_g} t \\ & - \frac{2}{3} \frac{D\eta}{P_f \rho_g} \rho_m (2C_0 + C_R) \log \left(\frac{\Delta P}{\eta} t \right) \end{aligned} \quad (A10)$$

where ρ_g is the gas density at $P = P_f$.

Appendix B

Numerical solution of the quasi-static and dynamic cases

The system of governing equations for the quasi-static approximation, including the effects of surface tension and finite separation (Eqs. (5), (9), and (13)), may be rewritten as:

$$\frac{dR}{dt} = V_R = \frac{1}{4\eta} \left(\frac{GT}{M} \rho_g - P_f - \frac{2\sigma}{R} \right) \frac{S_0^3 + R^3}{S_0^3} R \quad (B1)$$

$$\left(\frac{\partial C}{\partial r}\right)_R = \frac{S_0^3(C_0 - C_R) - \frac{\rho_g}{\rho_m} R^3}{S_0^3 R - \frac{3}{2} ((S_0^3 + R^3)^{2/3} - R^2) R^2} \quad (B2)$$

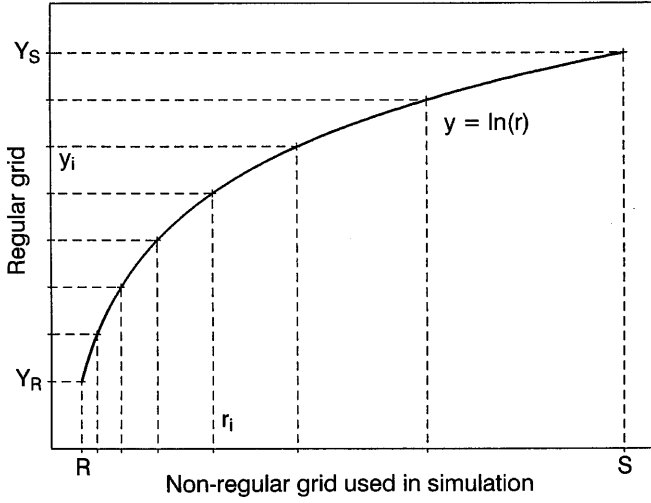


Fig. B1 Construction of the non-regular grid used for the simulation of the water concentration in a shell of melt of radius S surrounding a bubble of radius R (see text for explanation)

$$\frac{d\rho_g}{dt} = \frac{3D\rho_m}{R} \left(\frac{\partial C}{\partial r} \right)_R - \frac{3\rho_g V_R}{R} \quad (\text{B3})$$

This is a system of two first-order differential equations (Cauchy problem) for R and ρ_g and one algebraic equation for the gradient of water concentration at the bubble-melt interface. This system of equations requires two initial conditions. We assume that the bubble starts growing from a nucleus with radius $R_0 = 2R_{cr}$ with zero initial velocity ($V_R|_{t=0} = 0$). The second condition is derived from initial gas density:

$$\rho_g = \frac{M}{GT} \left(P_f + \frac{2\sigma}{R} \right) \quad (\text{B4})$$

Even for very low confining pressures, the Peclet number corresponding to the initial stage of growth is small and the quasi-static approximation may be applied. For high confining pressures the Peclet number remains small and the system of equations (Eqs. (B1)–(B4)) is integrated numerically for the full duration of the experiment, using a constant time step.

Simulation of bubble growth at low confining pressures also begins with the quasi-static solution. However, the Peclet number is calculated for each time step. When this number exceeds some critical value $Pe_{cr} = t_D/t_v = 0.01$ the simulation in the quasi-static regime is stopped and the simulation in the dynamic regime begins. All bubble parameters (R , V_R , ρ_g) calculated at the last time step of the quasi-static regime are the initial conditions for the dynamic regime. The initial distribution of water concentration for the dynamic regime is calculated according to the quasi-static solution (Eq. (11)).

Subsequently, the analytical solution for the gradient of water concentration at the bubble-melt interface (Eq. (B3)) cannot be used and Eq. (1) is solved nu-

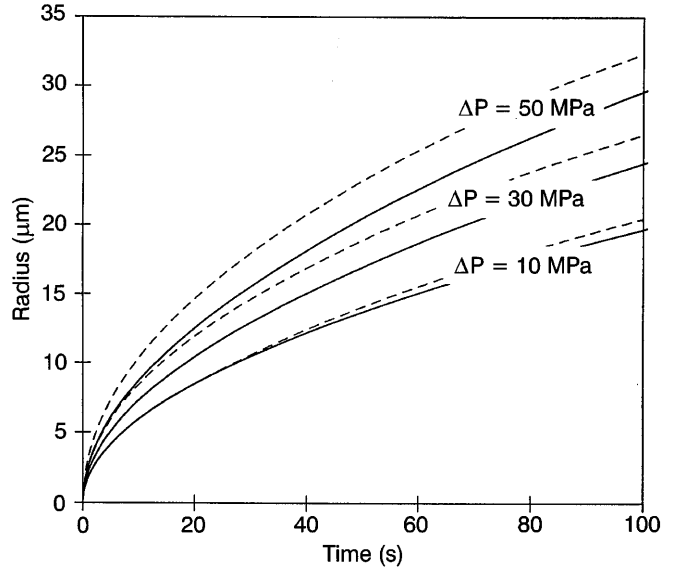


Fig. B2 Comparison of the dynamic (*dashed lines*) and quasi-static (*solid lines*) solutions for $\Delta P = 10, 30,$ and 50 MPa, $S = 200$ μm , and $D = 2 \times 10^{-11}$ m^2/s

merically in order to calculate the gradient for each time step. The numerical techniques of the solution of these type of equations require a finite grid for the time and spatial coordinate. The accuracy of the calculation of water concentration around the bubble is determined by the spatial step of the grid, which should be smaller than one bubble radius. If we were to use the regular mesh for large bubble separation ($S \gg R$), we would need a huge number of grid nodes and the calculations would be time-consuming. In order to reduce computer time without loss of accuracy, we used a non-regular mesh. This mesh was constructed by the projection of the simulation region ($R \leq r \leq S$) on the interval ($Y_R \leq y \leq Y_S$) by the function:

$$y = \ln(r)$$

A regular mesh is built in y -coordinates (Fig. B2) and each point of the y -mesh is projected back on the region of simulation:

$$R_i = \exp(Y_i)$$

where R_i and Y_i are grid points. For each time step the distribution of water concentration around the bubble may be represented as a Taylor series of the variable ($1/r$):

$$C(r) = a_0 + \frac{a_1}{r} + \frac{a_2}{r^2} + \frac{a_3}{r^3} + \dots \quad (\text{B5})$$

The finite difference approximation of the derivation ($\partial C/\partial r$) depends only on the discretization along the y -coordinate and does not increase with increasing interval of discretization along the r -coordinate. To show

this we take three nodes: R_{i-1} , R_i , R_{i+1} and calculate the first derivative as:

$$\left. \frac{\partial C}{\partial r} \right|_{r=R_i} = \frac{1}{2} \left[\frac{R_{i-1}}{R_i} \frac{C(R_i) - C(R_{i-1})}{R_i - R_{i-1}} + \frac{R_{i+1}}{R_i} \frac{C(R_{i+1}) - C(R_i)}{R_{i+1} - R_i} \right]$$

This approximation differs from the exact derivation of the Taylor series (Eq. (B5)) by terms of the order $(\Delta y)^2$, regardless of the corresponding ΔR .

In order to take into account viscous deformation of the melt around the bubble, we used the Lagrangian coordinate system, i.e., the coordinate of each grid point is changed according to the velocity of the melt (Eq. (4)). This transformation of coordinates eliminates the advective term from the diffusion in Eq. (1). Velocity of the melt decreases with distance from the bubble (Eq. (4)), which leads, on one hand, to a decrease in size of the simulation area (from the bubble interface to the surface of the shell), and on the other, to the increase of the non-uniformity of the grid. When the grid becomes too distorted, a new mesh with a reduced number of points is constructed. Interpolation from the old nodes to the new mesh must be done only at this stage. This is in contrast to the Eulerian method where such interpolation must be performed at each time step. The reduction in the number of nodes efficiently shortens computation time without diminishing the accuracy of the calculations.

In order to determine the maximum supersaturation pressure for which the quasi-static approximation may be applied, we ran two parallel simulations for the quasi-static and dynamic solutions using the following parameters $\Delta P = 30, 40, \text{ and } 50 \text{ MPa}$, $S = 200 \text{ }\mu\text{m}$, $\eta = 5 \times 10^4 \text{ Pa s}$, and $D = 2 \times 10^{-11} \text{ m}^2/\text{s}$. This lower value of D was preferred in order to overestimate the maximum possible error. At the initial stage of the bubble growth the numerical scheme of the dynamic solution follows the quasi-static approximation and both solutions coincide (Fig. B2). After a certain period, the advective term is also taken into account in the dynamic scheme and the two curves deviate. The results indicate that for ΔP smaller than 40 MPa ($P_f > 110 \text{ MPa}$), the effect of advective flux is small and the quasi-static approximation does not introduce any serious error.

Our simulations yield close agreement with the numerical results of Proussevitch et al. (1993) when run under similar conditions. The bench marking of the numerical scheme with the asymptotic solution (Eqs. (14) and (A10)) is shown in Fig. 2. The value R^2/t at each time step of the numerical solution is compared with the analytical solution for a range of supersaturation pressures of 10, 30, and 50 MPa. At supersaturation pressures of 10 and 30 MPa, the numerical and analytical solutions coincide after less than half a second and differ by less than 10% from the constant asymptotic value. At higher supersaturation pressures the analyti-

cal solution underestimates the radius. This result is expected as the effect of the advective flux, which enhances the rate of water transport, can no longer be ignored. This effect is obviously included in the numerical solution, leading to the larger calculated bubble radii. Simulation with $S \gg R$ yields an excellent agreement with the analytical solution of Scriven (1959), even at low pressures (Fig. 6). The difference between analytical and numerical solutions at $40 < P_f < 80 \text{ MPa}$ is due to the limitation of the polynomial approximation (Sparks 1978), which slightly overestimates Scriven's growth constant, β , at this interval.

Notation List

A, B	constants	
C	concentration	wt%
D	diffusion coefficient	m^2/s
G	Universal gas constant	$\text{J}/\text{mole} \times \text{ }^\circ\text{C}$
K_h	Henry's constant	$\text{Pa}^{0.5}$
m	mass of the gas in the bubble	kg
M	molecular weight of water	kg/mole
N_d	bubble number density	cm^{-3}
P	pressure	MPa
r	radial coordinate	μm
R	bubble radius	μm
S	separation	μm
t	time	s
T	temperature	$^\circ\text{C}$
v	radial melt velocity	m/s
V_R	bubble growth rate	m/s
ΔP	supersaturation pressure	MPa
β	Scriven's growth constant	
γ	surface element	m^2
η	melt viscosity	Pa s
ρ	density	kg/m^3
σ	surface tension	N/m

Subscripts

0	initial value
f	final value
g	gas
m	melt
r	radial coordinate
R	properties of the bubble melt interface

References

- Baker DR, Vaillancourt J (1995) The low viscosities of F + H₂O-bearing granitic melts and implications for melt extraction and transport. *Earth Planet Sci Lett* 132:199–211
- Bottinga Y, Javoy M (1990) MORB degassing: bubble growth and ascent. *Chem Geol* 81:255–270
- Burnham CW (1975) Water and magmas; a mixing model. *Geochim Cosmochim Acta* 39:1077–1084
- Cable M, Evans DJ (1967) Spherically symmetrical diffusion-controlled growth or dissolution of a sphere. *J Appl Phys* 38:2899–2906

- Chekhmir AS, Epel'baum EM, Simakin AG (1989) Transport of water in magmatic melts *Geokhymia* 2:303–305 (in Russian)
- Epel'baum MB, Babashov IV, Salova TP (1973) Surface tension of felsic magmatic melts at high temperatures and pressures. *Geokhimiya* 3:461–464 (in Russian)
- Epstein PS, Plesset MS (1950) On the stability of gas bubbles in liquid–gas solutions. *J Chem Phys* 18:1505–1509
- Fisher JR (1976) The volumetric properties of H₂O: a graphical portrayal. *J Res US Geo Survey* 4:189–193
- Holloway JR, (1977) Fugacity and activity of molecular species in supercritical fluids. In: Fraser DG (ed) *Thermodynamics in geology*. Reidel, Boston, pp 161–181
- Hurwitz S, Navon O (1994) Bubble nucleation in rhyolitic melts: experiments at high pressure, temperature and water content. *Earth Planet Sci Lett* 122:267–280
- Jaupart C, Allegre CJ (1991) Gas content, eruption rate and instabilities of eruption regime in silicic volcanoes. *Earth Planet Sci Lett* 102:413–429
- Jaupart C, Tait S (1990) Dynamics of eruptive phenomena. *Rev Mineral* 24:213–238
- Karsten JL, Holloway JR, Delaney JR (1982) Ion microprobe studies of water in silicate melts: temperature-dependent water diffusion in obsidian. *Earth Planet Sci Lett* 59:420–428
- Klug C, Cashman KV (1994) Vesiculation of May 18, 1980, Mount St. Helens magma. *Geology* 22:468–472
- Lapham KE, Holloway JR, Delaney JR (1984) Diffusion of H₂O and D₂O in obsidian at elevated temperatures and pressures. *J Non-Crystal Solids* 67:179–191
- Mangan MT, Cashman KV, Newman S (1993) Vesiculation of basaltic magma during eruption. *Geology* 21:157–160
- Murase T, McBirney A (1973) Properties of some common igneous rocks and their melts at high temperatures. *Geol Soc Am Bull* 84:3536–3592
- Papale P, Dobran F (1993) Modeling of the ascent of magma during the plinian eruption of Vesuvius in AD 79. *J Volcanol Geotherm Res* 58:101–132
- Persikov ES (1991) The viscosity of magmatic liquids: experiment, generalized patterns. A model for calculation and prediction. Applications. In: Perchuk PL, Kushiro I (eds) *Physical chemistry of magmas*. Springer, Berlin Heidelberg New York, pp 1–40
- Proussevitch AA, Sahagian DL, Anderson AT (1993) Dynamics of diffusive bubble growth in magmas: isothermal case. *J Geophys Res* 98 (22):283–307
- Readey DW, Cooper AR (1966) Molecular diffusion with a moving boundary and spherical symmetry. *Chem Eng Sci* 21:917–922
- Sahagian DL, Proussevitch AA, Anderson AT (1994) Reply on comment on “Dynamics of diffusive bubble growth in magmas: isothermal case”. *J Geophys Res* 99 (17): 829–832
- Scriven LE (1959) On the dynamics of phase growth. *Chem Eng Sci* 10:1–13
- Shaw HR (1972) Viscosities of magmatic silicate liquids: an empirical method of prediction. *Am J Sci* 272:870–893
- Silver LA., Ihinger PD, Stolper EM (1990) The influence of bulk composition on the speciation of water in silicate glasses. *Contrib Mineral Petrol* 104:142–162
- Sparks RSJ (1978) The dynamics of bubble formation and growth in magmas: a review and analysis. *J Volcanol Geotherm Res* 3:1–37
- Sparks RSJ (1994) Comment on “Dynamics of diffusive bubble growth in magmas: isothermal case”. *J Geophys Res* 99 (17): 827–828
- Sparks RSJ, Barclay J, Jaupart C, Mader HM, Phillips JC (1994) Physical aspects of magmatic degassing I. Experimental and theoretical constraints on vesiculation. *Rev Mineral* 30:413–445
- Szekely J, Fang SD (1973) Non-equilibrium effects in the growth of spherical gas bubbles due to solute diffusion. II. the combined effects of viscosity, liquid inertia, surface tension and surface kinetics. *Chem Eng Sci* 28:2127–2140
- Toramaru A (1989) Vesiculation process and bubble size distribution in ascending magmas with constant velocities. *J Geophys Res* 94 (17): 523–542
- Toramaru A (1990) Measurement of bubble size distribution in vesiculated rocks with implications for quantitative estimation of eruption process. *J Volcanol Geotherm Res* 43:71–90
- Wilson L, Sparks RSJ, Walker GPL (1980) Explosive volcanic eruptions. IV. The control of magma properties and conduit geometry on eruption column behavior. *Geophys J Astr Soc* 63:117–748
- Zak M, Weinberg MC (1980a) Gas diffusion in multibubble systems. *J Eng Sci* 35:1749–1754
- Zak M, Weinberg MC (1980b) Multibubble dissolution in glass melts. *J Non-Crystal Solids* 38:533–538
- Zhang Y, Stolper EM, Wasserburg GJ (1991) Diffusion of water in rhyolitic glasses. *Geochim Cosmochim Acta* 55:441–456